crystals

MDPI

Article

Corrosion Resistance and Modification Mechanism of Cement Mortar Containing Fly Ash and SAP Under Multi-Salt Coupling Conditions

Suining Zheng [1,2], Mingrui Sun [2], Zhihan Li [2], Anhua Xu [1,*] and Huaxin Chen [1,2,*]

[1] Qinghai Provincial Key Laboratory of Tibet Plateau Highway Construction and Maintenance Technology, Qinghai Polytechnic University, Xining 810003, China
[2] School of Materials Science and Engineering, Chang'an University, Xi'an 710061, China
* Correspondence: xahua@ghmu.edu.cn (A.X.); hxchen@chd.edu.cn (H.C.); Tel.: +86-137-5994-2198 (H.C.)

Abstract

To improve the durability of cement-based materials in multi-salt coupled corrosion environments, six cement mortar mixtures were designed. The fly ash content ranged from 10% to 40%, and the superabsorbent polymer (SAP) content ranged from 0% to 0.3%. Four corrosion environments were used: tap water, 10% NaCl solution, 10% $MgSO_4$ solution, and a 10% NaCl with 10% $MgSO_4$ composite solution. The degradation behavior and the modification mechanism of fly ash and SAP were investigated. Macroscopic tests were performed on apparent morphology, mass change, compressive strength, and flexural strength. Thermogravimetric and derivative thermogravimetric (TG/DTG) analysis and scanning electron microscopy (SEM) were also conducted. It was found that the damage caused by multi-salt coupling was much greater than that caused by single-salt corrosion. The damage severity decreased in the order of composite solution, $MgSO_4$ solution, NaCl solution, and tap water. The competitive adsorption, synergistic reactions, and mutual antagonism of Cl^-, SO_4^{2-}, and Mg^{2+} associated with large-area surface spalling, penetrating cracks, and mechanical strength loss. A parabolic trend was observed for the effect of fly ash content on corrosion resistance. The best balance between the filling effect and secondary hydration was obtained at a 20% content. The lowest mass loss and the highest compressive strength retention were obtained at this content. A 10% content was insufficient for modification. Corrosion resistance decreased at a 40% content because of the low clinker proportion. An optimal SAP content threshold of 0.2% was observed. With an appropriate SAP content, the pore size was refined, connected pores were blocked, and the expansion stress of corrosion products was buffered. Corrosion damage was thereby delayed. The microscopic analysis indicated that more expansive products were formed under the multi-salt environment. These products included ettringite, gypsum, and Friedel's salt. The C-S-H gel was also more severely damaged. With the combined addition of fly ash and SAP, the formation of corrosion products was reduced, the gel skeleton was protected, and a denser and more uniform microstructure was obtained. Therefore, a multiple protection system was formed by the combined addition of fly ash and SAP. This system involved physical blocking, chemical consumption, ion immobilization, and crack inhibition. The mixture with 20% fly ash and 0.2% SAP was the optimal mix proportion within the tested mixture series and exposure conditions. The durability of cement-based materials in the multi-salt coupled corrosion environment was improved within the tested mixture series and exposure conditions. An experimental basis for mix design and durability protection of cement-based materials in corrosive environments is provided by these findings.

Check for updates

Academic Editor: Raghvendra Singh Yadav

Received: 19 October 2026
Revised: 15 November 2026
Accepted: 16 November 2026
Published: 18 November 2026

Copyright: © 2026 by the authors. Licensee MDPI, Basel, Switzerland. This article is an open access article distributed under the terms and conditions of the Creative Commons Attribution (CC BY) license.

Keywords: cement mortar; corrosion resistance; fly ash; microstructure; multi-salt coupled corrosion; superabsorbent polymer (SAP); synergistic modification mechanism

1. Introduction

The groundwater and soil in coastal marine engineering areas and saline soil regions of northwest China are rich in corrosive ions, such as Cl^-, SO_4^{2-}, and Mg^{2+}. Cement-based materials in these areas are exposed to long-term multi-salt coupled corrosion. Surface spalling, cracking, and mechanical deterioration occur readily, and the durability and service safety of engineering structures are seriously threatened [1]. Conventional durability studies have mainly focused on single chloride or single sulfate attack. The established theories of ion transport and deterioration cannot accurately describe the complex damage process under multi-salt coexistence [2]. Conventional protective measures, such as increasing the strength grade or the cover thickness, cannot fundamentally inhibit the deep penetration and chemical reactions of multi-salt ions [3]. Therefore, the deterioration behavior of cement-based materials under multi-salt coupled corrosion must be clarified. Efficient modification and protection technologies must also be developed. These issues have become research hotspots for improving the durability of structures in saline soil and marine engineering [4].

The essence of multi-salt coupled corrosion is the competitive adsorption, synergistic reaction, and mutual antagonism of Cl^-, SO_4^{2-}, and Mg^{2+} between the pore solution and cement hydration products. The fastest migration rate was observed for Cl^-. It preferentially occupies adsorption sites in the pores and reacts with aluminum-bearing hydration products to form Friedel's salt. The early formation of ettringite is thereby inhibited [5]. SO_4^{2-} reacts continuously to form ettringite and gypsum. Expansive internal stress is generated, and microcracks are induced [6]. Ca^{2+} in the C-S-H gel is replaced by Mg^{2+} through ion exchange. Magnesium silicate hydrate with low cementitious activity is formed, and the gel skeleton is destroyed [7]. These processes are affected by the ion concentration ratio, pore structure, and material composition. The corrosion products also undergo dynamic formation and decomposition equilibria. As a result, the relationship between microscopic phase evolution and macroscopic performance deterioration is difficult to quantify. Calcium hydroxide can be consumed and the pores can be refined by fly ash through its filling effect and secondary hydration [8]. The pore structure can be optimized and the expansion stress can be buffered by SAP [9,10]. Synergistic protection is expected to be provided by the combined addition of fly ash and SAP [11]. However, the optimal proportion for environments with coupled Cl^-, SO_4^{2-}, and Mg^{2+} still requires investigation. The combined protection effect proposed above was not isolated experimentally in this study.

Recent studies have examined SAP and fly ash separately in cement-based systems. SAP dosage and mixing method affect flow, strength, and water retention [12], and SAP can reduce chloride ingress and permeability by refining the pore system and maintaining internal moisture [13,14]. Internal curing with SAP has also been applied to alkali-activated fly ash-slag pastes [15], and combined SAP-fly ash addition has been reported to alter mortar strength and microstructure [16]. For fly ash concrete under combined chloride-sulfate exposure, temperature and ion concentration affect the severity of deterioration [17], and coupled sulfate-chloride-magnesium attack can produce damage that is not reproduced by a single salt [18]; magnesium sulfate attack at low temperature causes distinct microstructural degradation [19]. The pore system formed by SAP may itself influence durability and drying shrinkage [20], and the absorption–desorption behavior of SAP in cement paste is a key factor controlling its effectiveness [21]. These studies provide a basis for the present work, but they do not establish a mix-design window for fly ash-SAP mortars exposed to

simultaneous Cl^-, SO_4^{2-}, and Mg^{2+} attack at low temperature. In particular, the individual and combined roles of fly ash and SAP, and the dose–response of SAP at a fixed fly ash content, remain unresolved.

In this study, P·O 42.5 ordinary Portland cement was used as the base material. Fly ash was used as the mineral admixture, and SAP was used as the functional admixture. Six cement mortar mixtures with different contents were designed. Four corrosion environments were used: tap water, 10% NaCl, 10% $MgSO_4$, and a 10% NaCl with 10% $MgSO_4$ multi-salt composite solution. Immersion corrosion tests were conducted on specimens cured for 7 d. Macroscopic tests were performed, including fluidity, apparent morphology, mass change, compressive strength, and flexural strength. TG/DTG and SEM characterization were also conducted. The degradation behavior of cement-based materials under multi-salt coupled corrosion and the modification effect of combined fly ash and SAP were compared. The internal relationship between ion competition and microstructure damage was analyzed. These results are expected to provide a basis for mix design and durability protection of cement-based materials in saline soil and marine engineering.

2. Materials and Methods

2.1. Raw Materials

P·O 42.5 ordinary Portland cement was used. ISO standard sand was used as the fine aggregate. Class I fly ash was used as the mineral admixture. SAP was used as the functional admixture, and its water absorption capacity in cement filtrate was 34 g/g. A high-performance polycarboxylate superplasticizer was used. Analytical grade NaCl and $MgSO_4$ with a purity of 99% were used as the corrosive reagents. Tap water was used as the mixing water. The cement and fly ash complied with the relevant Chinese standards for P·O 42.5 cement and Class I fly ash, respectively.

2.2. Mix Proportion Design

The cement, river sand, and mixing water were kept constant. The fly ash content was set at 10–40%. Three SAP contents of 0.1%, 0.2%, and 0.3% were used in the group with 20% fly ash. Six mixtures were designed and numbered R1 to R6. R1 was used as the reference group. The fluidity was measured by the flow table method. The superplasticizer content was adjusted so that the fluidity deviation of each group remained within ±5 mm. The influence of workability differences on the test results was thereby excluded. The mix proportions of cement mortar are shown in Table 1. The superplasticizer dosage was adjusted separately for each mixture (Table 1). Fly ash was added on top of the fixed cement content as an auxiliary mineral admixture. SAP dosage is expressed as mass per-centage of cement, the corresponding batch masses are 0.45, 0.90, and 1.35 g per 450 g of cement.

Table 1. Mix proportions of cement mortar (g).

Group	Cement	Fly Ash	River Sand	SAP	Superplasticizer	Water
R1	450	45	1350	0	0.9	184.5
R2	450	90	1350	0.45	3.6	184.5
R3	450	90	1350	0.90	5.4	184.5
R4	450	90	1350	1.35	5.4	184.5
R5	450	135	1350	0	7.2	184.5
R6	450	180	1350	0	7.2	184.5

2.3. Specimen Preparation and Curing

Raw materials were weighed according to the mix proportions and placed in a mortar mixer. The mixture was mixed at low speed for 30 s and at high speed for 90 s. The mortar was cast into 160 mm × 40 mm × 40 mm standard molds, compacted on a vibrating table, and leveled. The surface was covered with a film, and the specimens were left to stand. After 24 h, the specimens were demolded and placed in a constant-temperature and constant-humidity curing box (20 ± 2 °C, relative humidity ≥ 95%). Standard curing was continued to 7 d. After curing, the initial mechanical strength (MPa) of each specimen was recorded. The specimens were then dried in a constant-temperature oven at 60 °C to constant mass. The initial mass (g) was recorded. The 7 d curing period was the common baseline for all mixtures. The 60 °C drying step was used to obtain a stable reference mass for the mass-change measurement, it also reduced differences in initial moisture among specimens. All mixtures were treated identically so that the comparison remains internally consistent.

2.4. Corrosion Test Procedure

Four corrosion environments were used: a tap water control group, 10% NaCl solution, 10% $MgSO_4$ solution, and a 10% NaCl with 10% $MgSO_4$ composite multi-salt solution. The corrosion temperature was maintained at 10 °C. Static immersion was adopted. The specimens were corroded for 14 d and 28 d, respectively. The corrosion solution was replaced every 7 d to maintain a stable ion concentration.

2.5. Test Methods

2.5.1. Macroscopic Performance Tests

The fluidity of the mortar was measured by the flow table method. Surface spalling, cracks, efflorescence, and corner damage were visually observed and recorded before and after corrosion. The oven-dried mass was measured before and after corrosion, and the mass change rate was calculated. The compressive strength and flexural strength were tested with a computer-controlled electronic universal testing machine (TYE-2000B testing machine, Wuxi Jianyi Instrument Machinery Co., Ltd., Wuxi, China). Three parallel specimens were used for each group. The mechanical results are reported as arithmetic means of three specimens. Statistical significance tests were not performed.

2.5.2. Microscopic Characterization Tests

After the corrosion test, samples were taken from undamaged regions inside the specimens. The samples were ground and passed through an 80 μm standard sieve to prepare powder samples. TG/DTG tests were performed with a thermogravimetric analyzer (Q600 simultaneous thermal analyze, TA Instruments, New Castle, DE, USA) in a nitrogen atmosphere from 50 to 1000 °C. The microscopic morphology was observed with a Hitachi S-4800 cold field emission scanning electron microscope (Hitachi High-Technologies, Tokyo, Japan) at an accelerating voltage of 3.0 kV. Magnifications of ×5.00 k and ×10.0 k were used.

3. Results

3.1. Apparent Morphology

Apparent morphology is the most intuitive macroscopic manifestation of salt corrosion damage. The apparent characteristics of R3 specimens after 28 d of corrosion in different environments are listed in Table 2.

Table 2. Apparent morphology of R3 specimens after 14 d and 28 d of corrosion in different environments.

Corrosion Environment	Apparent Characteristics After 14 d	Apparent Characteristics After 28 d
Tap water control	The surface was flat, with no cracks or spalling. Only very slight efflorescence was observed at the edges.	The surface condition remained almost unchanged. The efflorescence area expanded slightly. No visible damage was observed.
10% NaCl (chloride)	The surface was basically intact, with no visible cracks. Pinhole-like micropores appeared locally. No spalling was observed.	The number of micropores increased slightly. No cracks or spalling were observed, and the edges remained intact.
10% $MgSO_4$ (sulfate)	Uniform white efflorescence appeared on the surface. A small amount of powdery spalling occurred at the edges. No visible cracks were observed.	Efflorescence intensified. Fine network-like microcracks appeared on the surface. The spalling depth at the edges was about 0.5–1.0 mm. No large-area peeling was observed.
10% NaCl with 10% $MgSO_4$ (multi-salt)	Efflorescence appeared on the surface. Blocky spalling occurred at the edges. Hair-like cracks were locally visible.	The surface mortar spalled in flakes to a depth of 1–2 mm, and internal sand particles were exposed. Multiple cracks with widths of 0.1–0.3 mm were present. The specimen edges were damaged, and local softening was observed.

It was found that the damage under multi-salt coupled corrosion developed much faster than that under single-salt corrosion. After 14 d of corrosion, edge spalling and microcracks had already appeared in the multi-salt group. After 28 d, the damage in the multi-salt group deteriorated sharply. The single-sulfate group was still dominated by fine network-like microcracks. Almost no cracks were found in the single-chloride group. The mixed solution produced greater damage than either single salt, which is consistent with a coupled effect among Cl^-, SO_4^{2-}, and Mg^{2+}.

3.2. Mass Change Behavior

3.2.1. Effect of Corrosion Solution Type on Mass Change

The mass change rate was determined by two competing effects. The first was mass gain from corrosion product formation and salt adsorption. The second was mass loss from surface mortar spalling. The initial masses of groups R1, R3, R5, and R6 were 551.33 g, 549.27 g, 548.49 g, and 551.3 g, respectively. The mass change rates of the specimens after 28 d in different corrosion environments are shown in Figure 1. In tap water, the mass change in each group was less than 3%. This result indicates that the mass of the cement-based material was basically stable without corrosive ions. In the single-chloride environment, obvious mass loss was observed in groups R3 and R5. This result indicates that immersion in the salt solution caused softening and spalling of the surface mortar. In the single-sulfate environment, a mass loss trend was observed in all groups except R1. The mass loss of R5 was the most significant, which was consistent with its larger spalling area. Under multi-salt coupling, the mass change varied greatly among the groups. A large mass gain (+2.07%) was observed in group R1. This gain was caused by the filling of pores by a large amount of corrosion products. However, this densification was only apparent, and expansion stress had already accumulated inside the specimen. A large mass loss (−5.64%) was observed in group R5, indicating insufficient matrix strength and large-area surface spalling. The smallest mass change (−1.45%) was observed in group R3. This result indicates a dynamic balance between corrosion product formation and surface spalling, as well as the best overall performance

among the tested mixtures. It should be noted that mass change is a net value, it cannot by itself distinguish the mass gain caused by corrosion product formation and salt uptake from the mass loss caused by spalling.

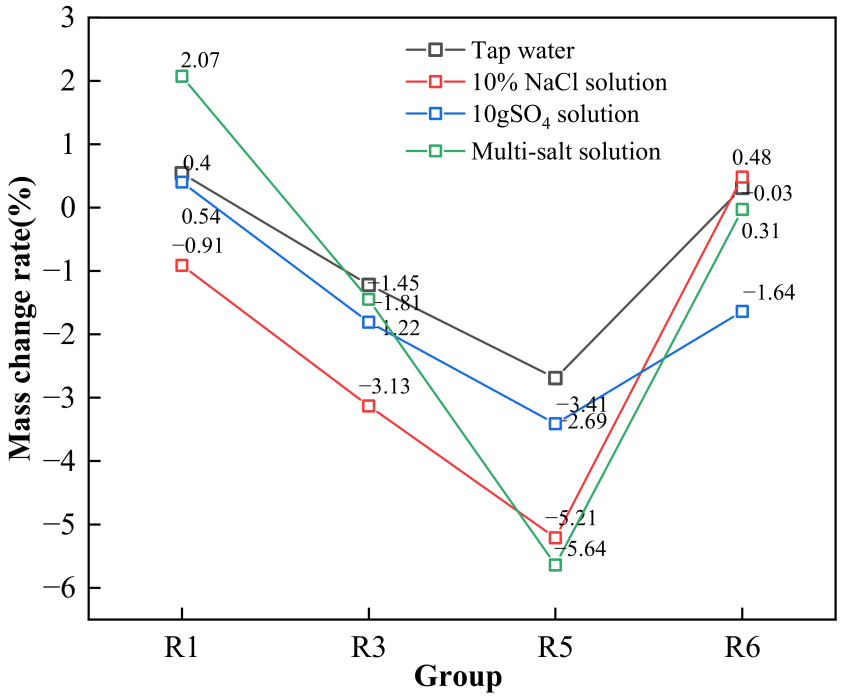


Figure 1. Mass change rate of specimens after 28 d in different corrosion solutions.

3.2.2. Effect of Fly Ash Content on Mass Change

The initial masses of R1, R3, R5, and R6 were 551.33 g, 549.27 g, 548.49 g, and 551.3 g, respectively. The mass change rates of the specimens with different fly ash contents after 28 d are shown in Figure 2. Under the 28 d multi-salt coupling condition, the effect of fly ash content on mass change showed a pattern of stability at both ends and divergence in the middle. A mass increase of 2.07% was observed in group R1 (10% fly ash). The high porosity and pore filling by corrosion products caused significant mass gain. However, the compressive strength retention was only 95.7%, indicating a strong surface but a weak interior. A mass decrease of 1.45% was observed in group R3 (20% fly ash). The combined filling and secondary hydration effects densified the structure. The formation and spalling of corrosion products reached a balance. This group had the highest mechanical retention and the best overall performance. A mass loss of 5.64% was observed in group R5 (30% fly ash). The clinker proportion decreased to 70%, hydration at 7 d was insufficient, and the interfacial transition zone was weak. Expansion cracking and large-area surface spalling were caused by multi-salt ions, and the brittleness increased significantly. The mass of group R6 (40% fly ash) remained almost unchanged, but large-area flaky spalling had already appeared on the surface. The surface was densified by the high fly ash content, and the mass gain from salt adsorption offset the mass loss from spalling. These results indicate that internal damage cannot be accurately reflected by a single mass change index. Apparent morphology and mechanical properties should also be considered.

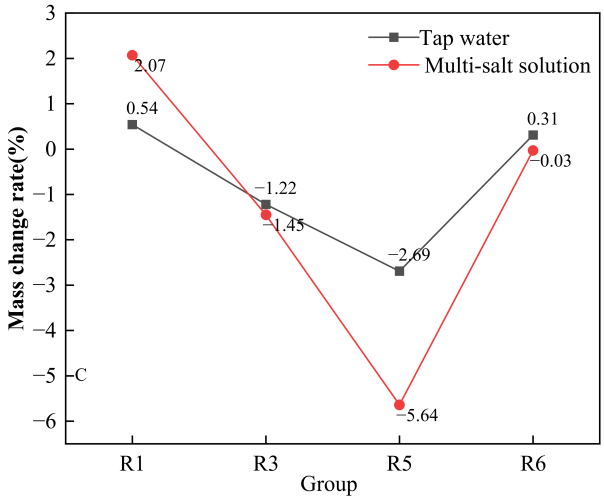


Figure 2. Mass change rate of specimens with different fly ash contents after 28 d under multi-salt coupling.

3.2.3. Effect of SAP Content on Mass Change

The initial masses of R2, R3, and R4 were 548.86 g, 549.27 g, and 549.65 g, respectively. The mass change rates of the specimens with different SAP contents after 28 d are shown in Figure 3. With a fixed fly ash content of 20%, the mass change rates after 28 d of multi-salt coupling differed significantly among the SAP contents. A mass change of −2.17% was observed in group R2 (0.1% SAP). Gel nodes were formed only locally by the low SAP content, the pore structure optimization was limited, and surface spalling was not sufficiently inhibited. A mass change of −1.45%, the smallest mass loss, was observed in group R3 (0.2% SAP). Uniform microgel spheres were formed by water absorption and swelling of an appropriate SAP content. The pore size was refined, ion transport channels were blocked, and expansion stress was buffered. Microcrack propagation and surface spalling were thereby effectively inhibited. A mass change of −3.25% was observed in group R4 (0.3% SAP), and the mass loss increased significantly. Large pores with diameters greater than 100 μm were formed in the matrix by excessive SAP. These pores became rapid ion transport channels. Abundant corrosion products were thereby formed around the pores, local stress concentration occurred, and surface spalling was induced. The internal-curing effect of SAP was inferred from the mass, strength, and SEM results.

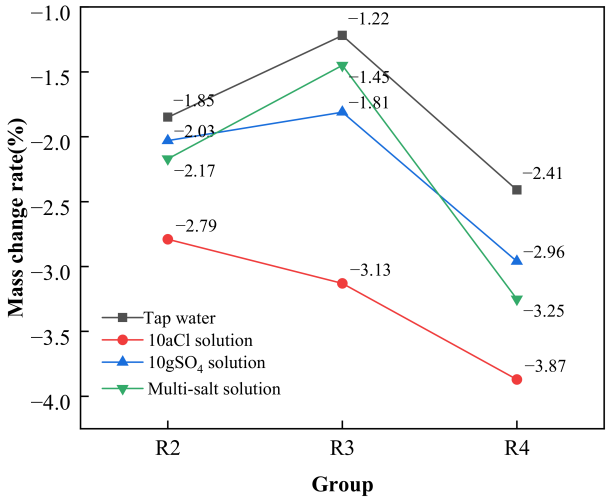


Figure 3. Mass change rate of specimens with different SAP contents after 28 d of corrosion.

3.3. Mechanical Property Deterioration

3.3.1. Effect of Corrosion Solution Type on Mechanical Properties

The measured compressive strengths of the specimens after 28 d in different corrosion environments are shown in Figure 4.

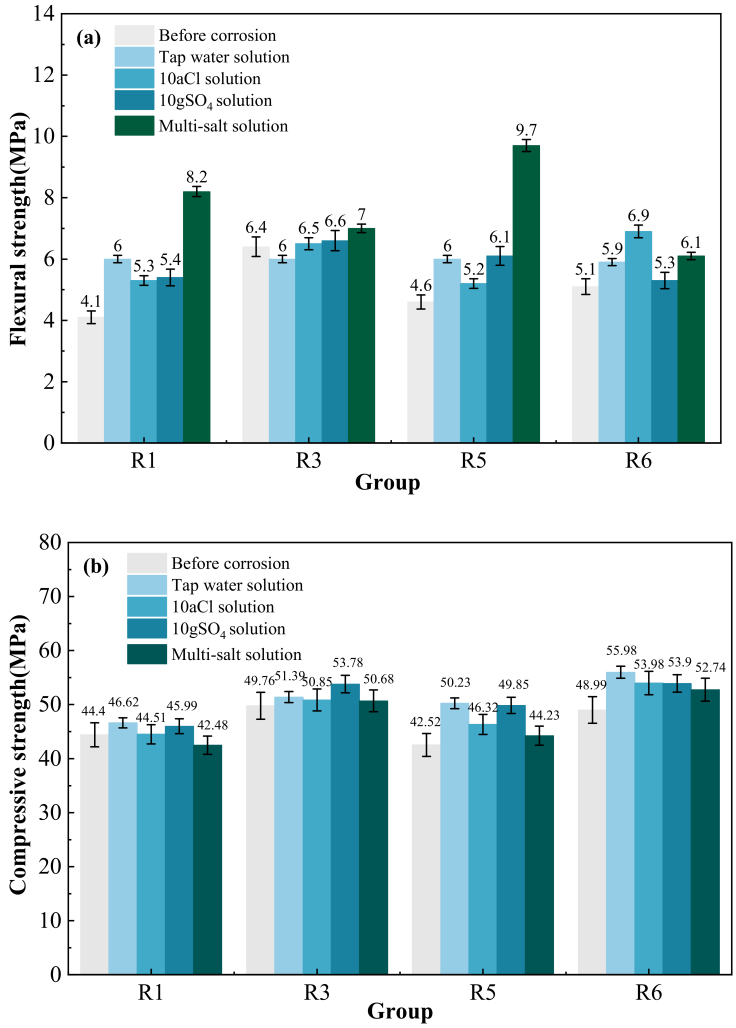


Figure 4. Mechanical strength of specimens under different corrosion environments. (**a**) Flexural strength. (**b**) Compressive strength.

As shown in Figure 4, the compressive strength of most specimens increased during the short-term corrosion stage from 14 to 28 d. This was a stage dominated by hydration and filling by corrosion products. Under multi-salt coupling, however, the compressive strength of group R1 decreased from 44.40 MPa to 42.48 MPa. The retention rate was about 95.7%. A compressive strength of 50.68 MPa was obtained in group R3 after corrosion, with a retention rate of about 101.8% relative to the 7 d pre-immersion strength of 49.76 MPa (Figure 4b). This group showed the best stability. Flexural strength was more sensitive to microcracks. Under the multi-salt environment, the flexural strengths of groups R1 and R5 increased considerably in the short term. However, the flexural-to-compressive strength ratio decreased. The brittleness of the material increased, and a hidden risk of deterioration existed.

3.3.2. Effect of Fly Ash Content on Mechanical Properties

The measured compressive strengths of the specimens with different fly ash contents after 28 d are shown in Figure 5. A parabolic trend, high in the middle and low at both ends, was observed for the effect of fly ash content on the mechanical properties under multi-salt corrosion. The overall performance was best at a 20% content. Group R1 (10% fly ash) showed insufficient modification, incomplete secondary hydration, and a relatively high matrix porosity. Its compressive strength retention after multi-salt corrosion was only 95.7%. The best combined effect between physical filling and secondary hydration was observed in group R3 (20% fly ash). It had the highest initial compressive strength, the strength retention closest to 100% after corrosion, and the best structural uniformity. In group R5 (30% fly ash), the cement clinker proportion decreased, and hydration was insufficient after 7 d of curing. This group had the lowest initial compressive strength. Although the strength was slightly increased by short-term filling by corrosion products, the brittleness increased and the long-term risk was high. In group R6 (40% fly ash), the filling effect was enhanced and the initial strength recovered. However, secondary hydration remained insufficient, and the long-term stability was inadequate. These statements refer to the trends observed within 28 d and are not long-term predictions.

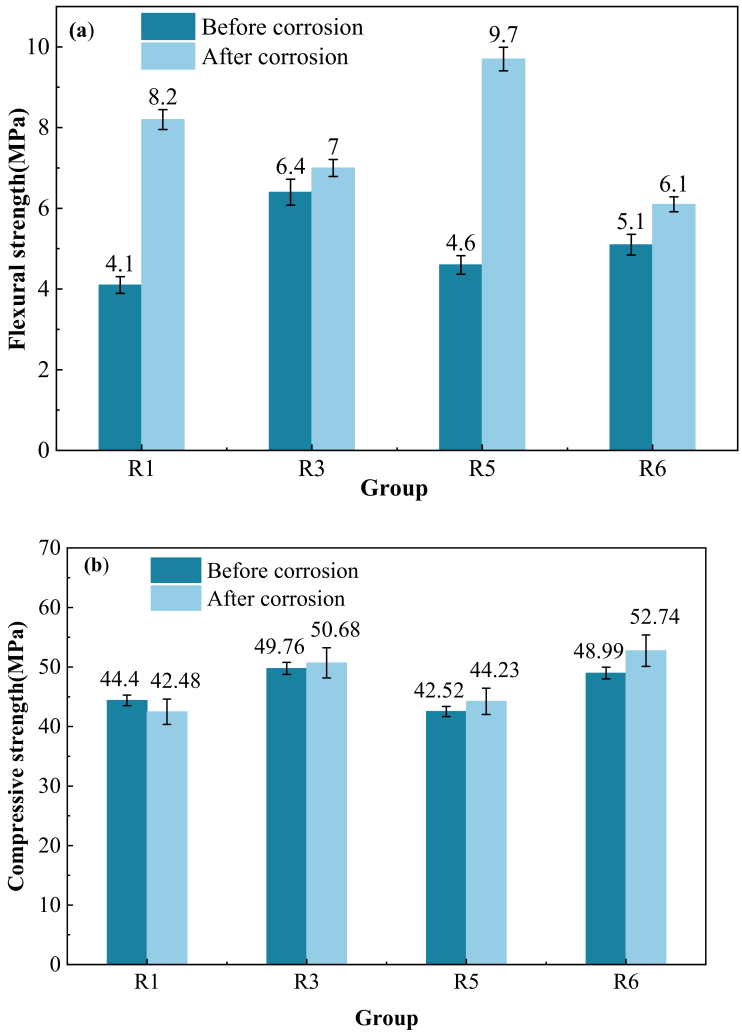


Figure 5. Mechanical strength of specimens with different fly ash contents. (**a**) Flexural strength. (**b**) Compressive strength.

3.3.3. Effect of SAP Content on Mechanical Properties

With a fixed fly ash content of 20%, the mechanical properties of the specimens with different SAP contents after 28 d of multi-salt corrosion are shown in Figure 6.

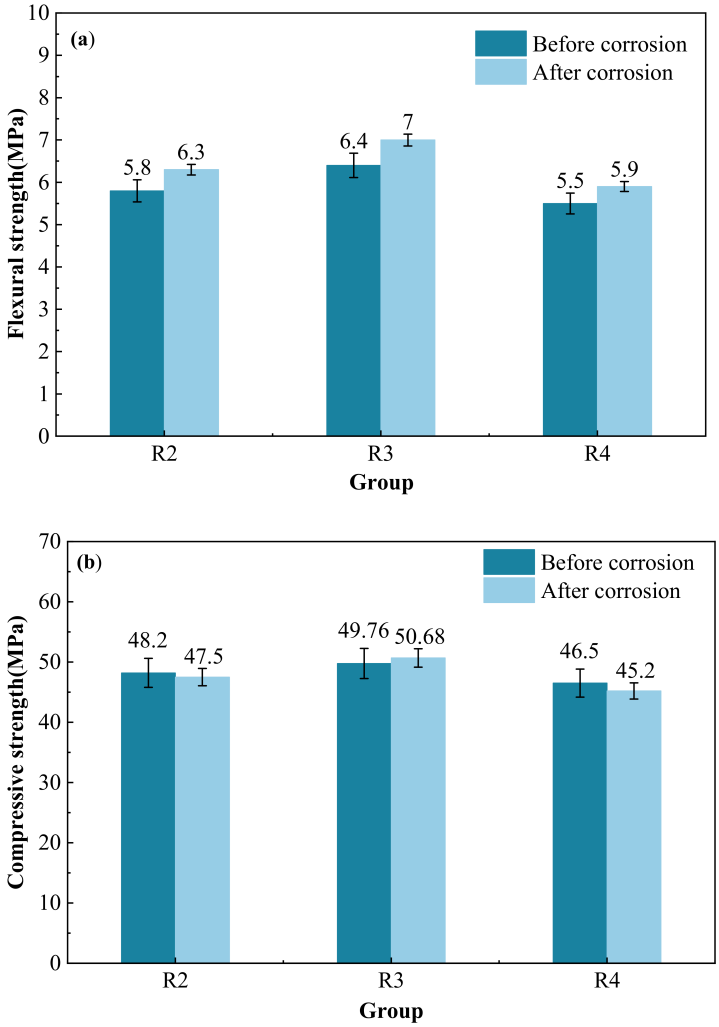


Figure 6. Mechanical strength of specimens with different SAP contents. (**a**) Flexural strength. (**b**) Compressive strength.

As shown in Figure 6, the modification effect of 0.1% SAP was not obvious. Gel nodes were formed only locally by the low SAP content, and the effect on pore structure optimization was limited. The best combined effect between 0.2% SAP and fly ash was observed. The pore size was refined, connected pores were cut off, and expansion stress was buffered. The compressive strength after corrosion remained higher than the initial strength.

3.4. Microstructure and Deterioration Mechanism Analysis

3.4.1. TG/DTG

The TG/DTG test results are shown in Figures 7–9. Figure 7 compares the thermogravimetric curves obtained in different corrosion solutions. The mass loss of the multi-salt group was significantly higher than that of the single-salt groups and the tap water group in all temperature ranges. In the range of 50–200 °C, the mass loss of the multi-salt group reached 18.2%, indicating the formation of more corrosion products containing crystal water. In the range of 200–400 °C, the strongest endothermic peak of the multi-salt group appeared at

about 280 °C, with a mass loss of 5.3%. This value was higher than those of the single-sulfate group (4.1%) and the single-chloride group (3.2%). This result indicates that the combined action of sulfate and magnesium salts increased the total amount of corrosion products. In the range of 400–600 °C, the mass loss of calcium hydroxide (CH) in the multi-salt group was the lowest, only 2.5%. This result indicates that CH was consumed by corrosive ions and further consumed by the secondary hydration of fly ash. In the range of 600–800 °C, the mass loss of the multi-salt group was the largest, reaching 4.7%. The decomposition peak of C-S-H gel shifted. This result indicated that Mg^{2+} destroyed the C-S-H gel structure through ion exchange and formed magnesium silicate hydrate gel with lower thermal stability. The mass losses of the single-chloride and single-sulfate groups in each range were between those of the tap water group and the multi-salt group. This result indicates that single-salt corrosion caused less damage than multi-salt coupled corrosion. The smallest mass loss was observed in the uncorroded 7 d specimen. This result indicates a low degree of hydration and few hydration products in the 7 d specimens. The 600–800 °C interval overlaps with the decomposition of carbonate phases and cannot be attributed exclusively to C-S-H gel. The shift in the DTG peak is consistent with Mg^{2+}-induced degradation of C-S-H.

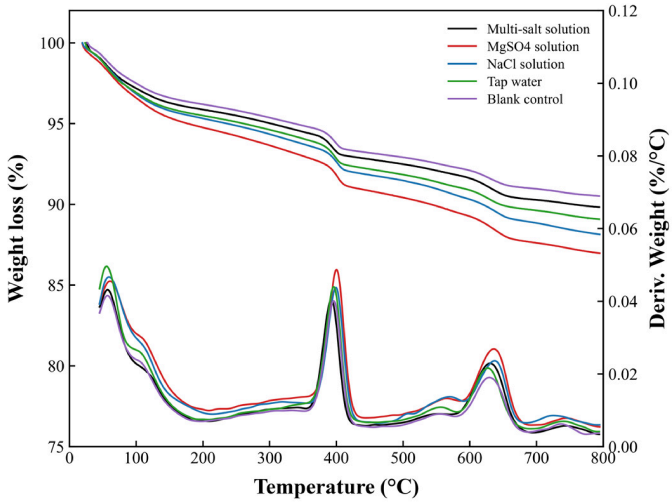


Figure 7. Thermogravimetric analysis of hydration products in different corrosion solutions.

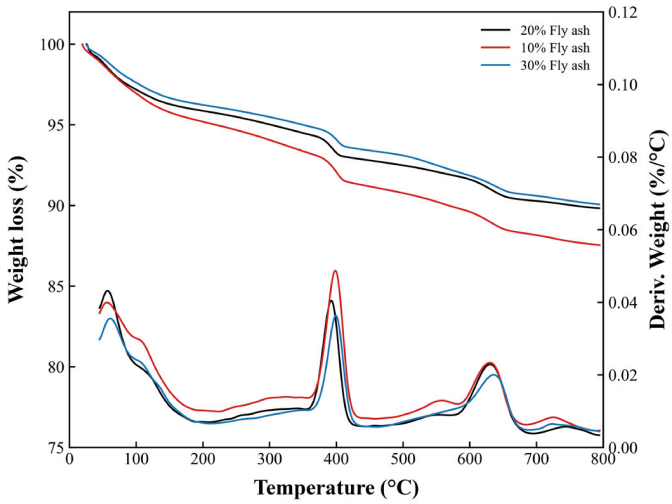


Figure 8. Thermogravimetric comparison of specimens with different fly ash contents.

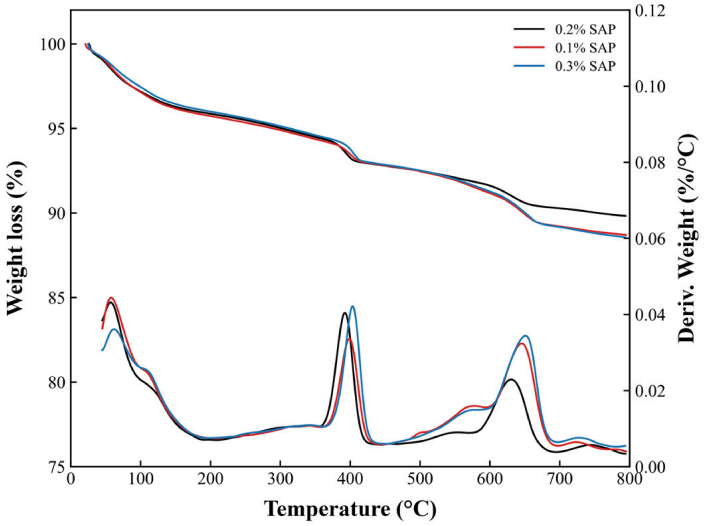


Figure 9. Thermogravimetric comparison of specimens with different SAP contents.

Figure 8 compares the thermogravimetric curves of hydration products with different fly ash contents. The fly ash content had a parabolic effect on phase evolution. Group R1 (10% fly ash) showed the largest mass loss in each range: 19.1% at 50–200 °C, 5.9% at 200–400 °C, and 3.1% for CH. This result indicates a high matrix porosity and the largest amount of corrosion products. The mass losses of group R3 (20% fly ash) decreased significantly in each range. The values decreased to 16.8% at 50–200 °C and 4.2% at 200–400 °C, and the CH loss was only 2.2%. The decomposition peak of C-S-H gel was close to that of the tap water group. Group R5 (30% fly ash) was between R1 and R3. This result indicates that an excessively low clinker proportion led to insufficient early hydration and a decrease in corrosion resistance.

Figure 9 compares the thermogravimetric curves of specimens with different SAP contents. An optimal SAP content was also observed. Group R4 (0.3% SAP) showed the largest mass loss in each range: 17.9% at 50–200 °C and 4.9% at 200–400 °C. This result indicates that excessive SAP formed large pores and accelerated ion penetration and corrosion reactions. Group R3 (0.2% SAP) showed the smallest mass loss in each range: 16.8% at 50–200 °C, 4.2% at 200–400 °C, and only 2.2% for CH. Its C-S-H structure was the most stable. These results indicate that an appropriate SAP content effectively optimized the pore structure, blocked ion transport channels, and buffered the expansion stress of corrosion products. The formation of corrosion products was thereby reduced, and the cementitious skeleton was protected. The mass losses of group R2 (0.1% SAP) were between those of R3 and R4. This result indicates that a low SAP content only formed gel nodes locally, could not fully optimize the pore structure, and had a limited inhibitory effect on ion penetration.

3.4.2. SEM

Figure 10 shows the SEM morphology of the uncorroded 7 d specimen (R3) and the tap water control group (R3). A loose matrix structure was observed in the uncorroded 7 d specimen, with weak bonding between particles, many connected pores, obvious cracks, and few hydration products. A noticeably denser structure was observed in the tap water group. Many needle-like and columnar crystals grew in an interlaced manner, and the pores were filled with C-S-H gel.

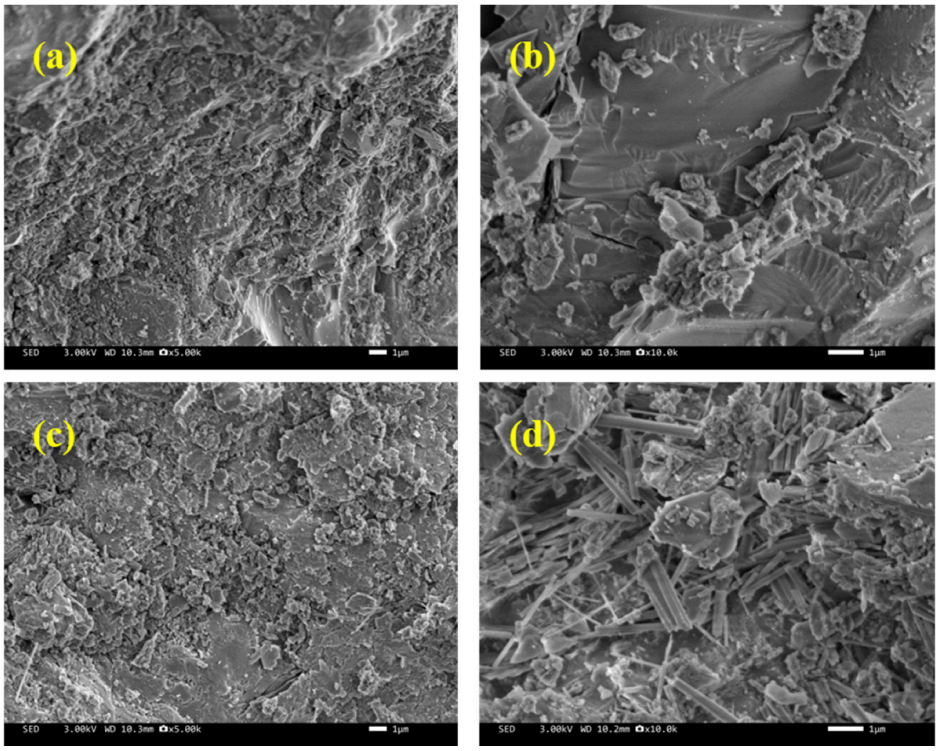


Figure 10. SEM morphology. (**a**) ×5.00 k, blank group; (**b**) ×10.00 k, blank group; (**c**) ×5.00 k, tap water group; (**d**) ×10.00 k, tap water group.

Figure 11 shows the SEM morphology of R3 in single-salt solutions and in the composite salt solution. Good compactness of the matrix was maintained in the 10% NaCl single-chloride environment. The number of pores increased slightly, and short columnar Friedel's salt was observed filling small capillary pores. The C-S-H gel structure remained basically intact, which was consistent with the slight strength increase in the specimens in the chloride environment. In the 10% $MgSO_4$ single-sulfate environment, the compactness of the matrix decreased, and the number and size of pores increased. Microcracks of 0.1–0.2 μm appeared. Needle-like ettringite and platy gypsum grew randomly in the pores and cracks. The expansive internal stress induced microcracks, which was the microscopic cause of apparent efflorescence and edge spalling. Under multi-salt coupling, the compactness of the matrix decreased further, the number of pores increased, and a few microcracks shorter than 10 μm appeared. Long needle-like ettringite and short needle-like Friedel's salt grew together. The ettringite was shorter and slightly less abundant than that in the single-sulfate group. This result is consistent with the inhibitory effect of Cl^- on ettringite formation. Slight loosening of the C-S-H gel was observed in some regions, indicating that Mg^{2+} had begun to destroy the gel skeleton. Phase identification in this study is based on morphology alone. XRD and SEM–EDS were not performed, so the assignments of ettringite, gypsum, Friedel's salt, and magnesium silicate hydrate are tentative.

The SEM morphology of the 10% fly ash group (R1) and the 30% fly ash group (R5) is shown in Figure 12. A loose matrix was observed in group R1, with many coarse pores larger than 10 μm and penetrating cracks. The ettringite crystals were abnormally coarse, with lengths of up to 8–10 μm. Many unhydrated particles were present, and the interfacial transition zone was weak. In contrast, group R3 (20% fly ash) in Figure 11 had a dense matrix, fine pores that were mostly closed, and corrosion products mainly filling capillary pores without obvious crystal accumulation. The compactness of group R5 was lower than that of R3. Many microcracks of 10–20 μm appeared, and relatively large hexagonal plate-

like CH crystals were observed. These results indicate insufficient secondary hydration and a loose C-S-H gel.

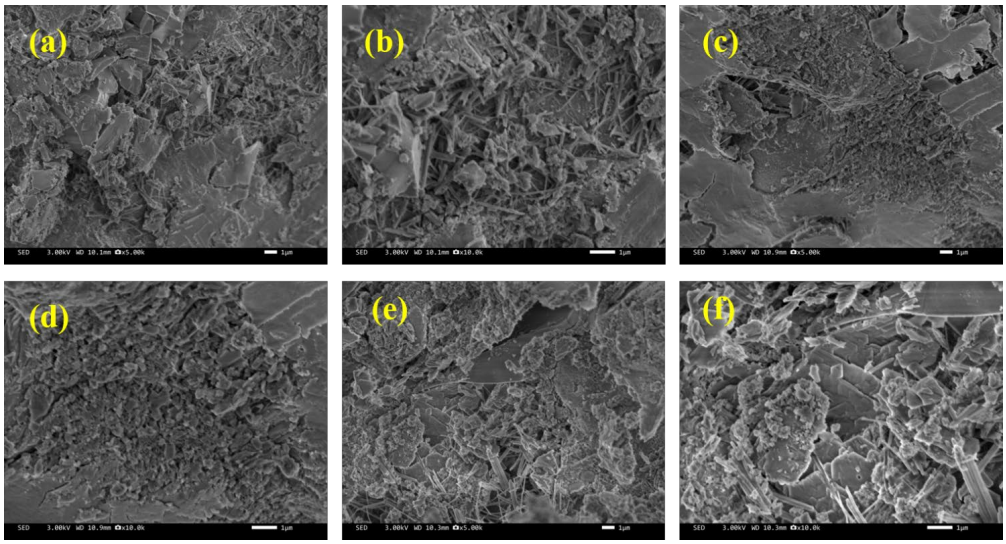


Figure 11. SEM morphology. (**a**) ×5.00 k, chloride; (**b**) ×10.00 k, chloride; (**c**) ×5.00 k, sulfate; (**d**) ×10.00 k, sulfate; (**e**) ×5.00 k, composite solution; (**f**) ×10.00 k, composite solution.

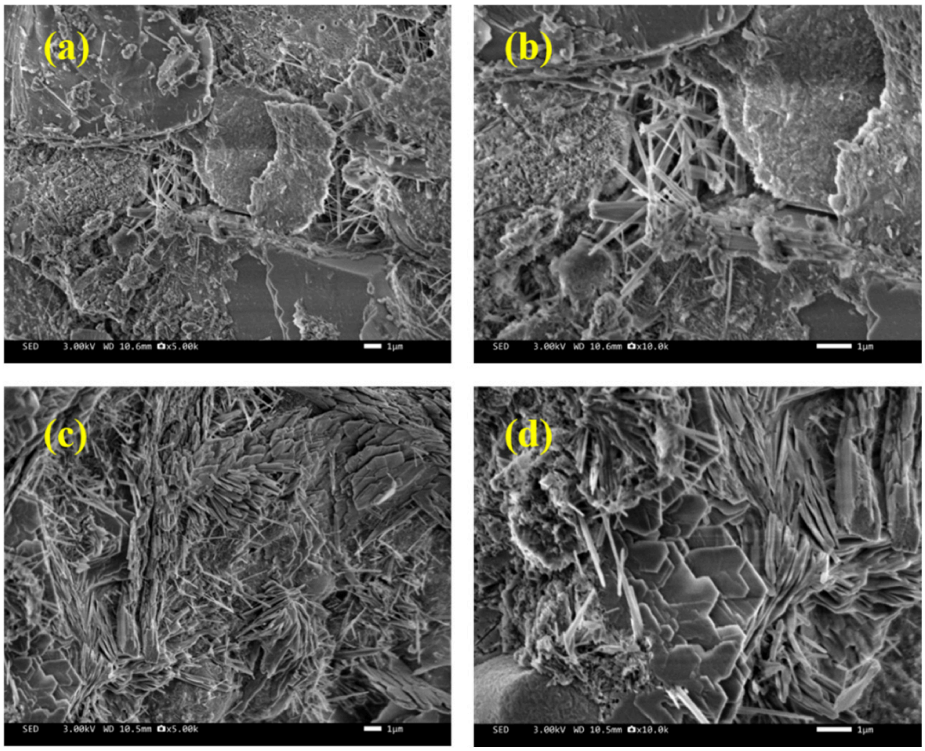


Figure 12. SEM morphology. (**a**) ×5.00 k, 10% fly ash; (**b**) ×10.00 k, 10% fly ash; (**c**) ×5.00 k, 30% fly ash; (**d**) ×10.00 k, 30% fly ash.

The SEM morphology of group R2 (0.1% SAP), group R3 (0.2% SAP), and group R4 (0.3% SAP) is shown in Figure 13. Many fine pores and microcracks were observed in group R2, and the corrosion products were unevenly distributed. Many large pores with diameters greater than 100 μm were observed in group R4. Radial microcracks appeared around these pores, ettringite and Friedel's salt crystals accumulated in the large pores, and the C-S-H gel around the cracks showed obvious loosening and damage. In contrast, group R3 in

Figure 11 had a dense matrix with fine and uniform pores. The microgel spheres formed by water absorption and swelling of SAP refined the pore size and blocked connected pores, and the corrosion products were uniformly distributed.

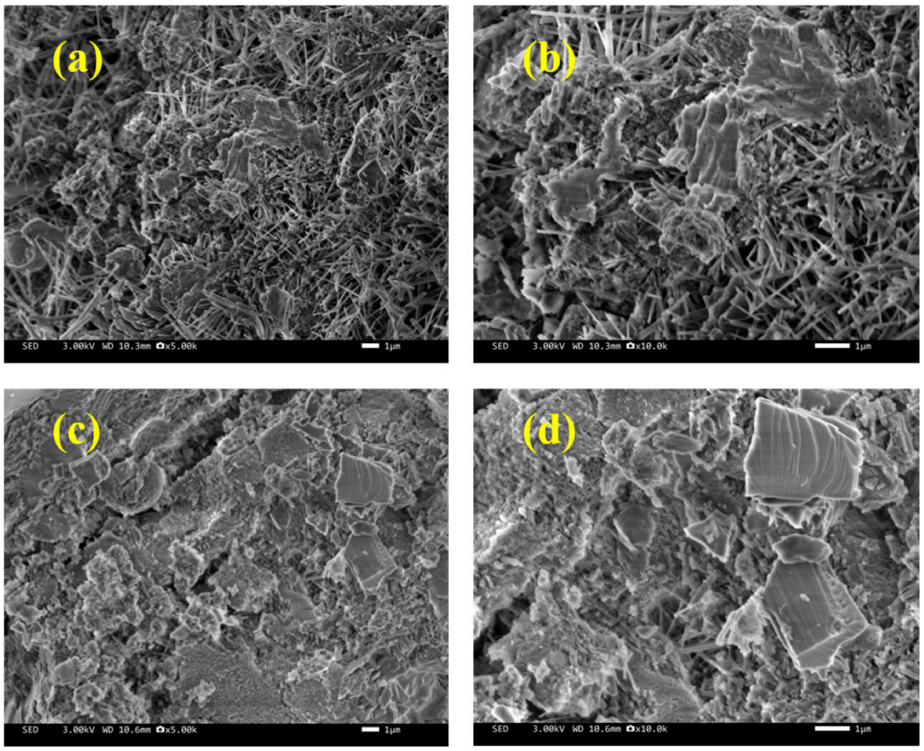


Figure 13. SEM morphology. (**a**) ×5.00 k, 0.1% SAP; (**b**) ×10.00 k, 0.1% SAP; (**c**) ×5.00 k, 0.3% SAP; (**d**) ×10.00 k, 0.3% SAP.

4. Protection Mechanism of Fly Ash and SAP

Under multi-salt coupled corrosion, the deterioration of cement-based materials is caused by the combined action of Cl^-, SO_4^{2-}, and Mg^{2+}. The fastest migration rate was observed for Cl^-. It preferentially occupies adsorption sites in the pores and inhibits the deep migration of SO_4^{2-}. Friedel's salt is formed by its reaction with aluminum-bearing hydration products, and the raw material for ettringite formation is consumed. Ettringite and gypsum are continuously formed by SO_4^{2-}, and expansive internal stress is generated. Microcracks are thereby induced. Ca^{2+} in the C-S-H gel is replaced by Mg^{2+} through ion exchange, and magnesium silicate hydrate with low cementitious activity is formed. The gel skeleton is destroyed. The dynamic formation and decomposition of corrosion products cause the microstructure to develop from local damage to penetrating cracks and surface spalling.

Corrosion resistance is improved by fly ash through three mechanisms. First, capillary pores are filled by fine spherical particles, the particle size distribution is optimized, and the initial porosity is reduced. Second, a secondary hydration reaction with CH is caused by the pozzolanic activity of fly ash. More C-S-H gel is formed, and CH, a core reactant in corrosion reactions, is consumed. Third, Cl^-, SO_4^{2-}, and Mg^{2+} are physically adsorbed and chemically immobilized, and the deep migration of harmful ions is inhibited. Crack resistance and corrosion resistance are improved by SAP through optimization of the pore structure, blocking of seepage channels, buffering of the expansion stress of corrosion products, and inhibition of microcrack propagation. A proposed multiple protection system involving physical blocking, chemical consumption, ion immobilization, and crack inhibition

is formed by the combined addition of fly ash and SAP. Within the 28 d exposure period, the durability of the tested mortars was improved by the combined addition of fly ash and SAP.

5. Conclusions

(1) The deterioration damage caused by multi-salt coupled corrosion was significantly greater than that caused by single-salt corrosion. The damage severity of the four corrosion environments decreased in the order of multi-salt composite solution, single $MgSO_4$ solution, single NaCl solution, and tap water. Under the multi-salt environment, competitive adsorption, synergistic reactions, and mutual antagonism were observed among Cl^-, SO_4^{2-}, and Mg^{2+}. These effects appeared macroscopically as large-area surface spalling, penetrating cracks, accelerated mass loss, and decreased mechanical strength.

(2) A parabolic trend was observed for the effect of fly ash content on the multi-salt corrosion resistance of cement-based materials. A 10% content was insufficient for modification. At 20% content, the filling effect and secondary hydration of fly ash acted together. The pore structure was significantly optimized, and CH was consumed. At a 40% content, the cement clinker proportion was too low, the early strength of the matrix was insufficient, and the corrosion resistance decreased. The overall performance was best at a 20% fly ash content. This optimum applies to the tested fly ash series.

(3) An optimal SAP content threshold of 0.2% was observed. With an appropriate SAP content, the pore size was refined, connected pores were blocked, expansion stress was buffered, and microcrack propagation was inhibited. Large pores and weak interfaces were introduced by excessive SAP, and corrosion damage was accelerated. Within the tested mixture series and the 28 d exposure conditions (10 °C static immersion in 10% NaCl, 10% MgSO4, and their mixture), the mixture with 20% fly ash and 0.2% SAP showed the best overall performance.

(4) The microscopic phase evolution under multi-salt corrosion was highly correlated with the macroscopic performance deterioration. According to the TG/DTG and SEM results, higher contents of expansive products, such as ettringite, gypsum, and Friedel's salt, were formed under the multi-salt environment, and the C-S-H gel was more severely damaged. With the combined addition of fly ash and SAP, the formation of corrosion products was reduced, and the C-S-H gel structure was protected. A denser and more uniform microstructure was obtained, and the macroscopic mechanical properties and volume stability were improved. The phase assignments are based on SEM morphology and TG/DTG mass-loss ranges.

The present study is a short-term comparative test. In future work, a full factorial design should be adopted to investigate the individual and coupled effects of fly ash, SAP, and the water-to-binder ratio. The exposure duration should be extended, and wet–dry/temperature cycles, variable salt concentrations, and mechanical loading should be introduced. Through XRD/EDS, MIP, and ion-penetration tests, a quantitative relationship among microstructure, ion transport, and macroscopic performance should be established so that a basis for service-life prediction in multi-salt environments can be provided.

Author Contributions: Conceptualization, S.Z. and H.C.; methodology, S.Z., A.X. and H.C.; validation, M.S. and Z.L.; formal analysis, S.Z.; investigation, A.X. and H.C.; resources, A.X. and H.C.; writing—original draft preparation, S.Z., M.S. and Z.L.; writing—review and editing, S.Z.; supervision, A.X. and H.C.; funding acquisition, S.Z. All authors have read and agreed to the published version of the manuscript.

Funding: This research is supported by the Open Foundation of the Key Laboratory for Highway Construction and Maintenance on the Qinghai-Tibet Plateau, Qinghai Province (2024-JY-D-02), the Key R&D and Transformation Program of Qinghai Province (2025-GX-109), and the Postdoctoral Research Project of Shaanxi Province (2025BSHSDZZ266).

Data Availability Statement: The data that support the findings of this study are available from the corresponding authors upon reasonable request.

Conflicts of Interest: The authors declare no conflicts of interest.

References

1. Tian, H.; Zhang, Y.; Feng, Q.; Qiao, H.; Xue, C.; Zhu, X. Time-dependent pore structure evolution and durability life prediction of polymer-modified manufactured sand concrete in western China's saline environment. *Constr. Build. Mater.* **2026**, *515*, 145632. [CrossRef]
2. Abd El Fattah, A.M.; Amao, A.O.; Riding, K.; Kawde, A. Durability of fly ash and limestone concrete under combined sulfate and chloride attack. *Int. J. Concr. Struct. Mater.* **2026**, *20*, 16. [CrossRef]
3. Meng, Z.; Liu, Q.; Ukrainczyk, N.; Mu, S.; Zhang, Y.; De Schutter, G. Numerical study on the chemical and electrochemical coupling mechanisms for concrete under combined chloride-sulfate attack. *Cem. Concr. Res.* **2024**, *175*, 107368. [CrossRef]
4. Liu, Q. Progress and research challenges in concrete durability: Ionic transport, electrochemical rehabilitation and service life prediction. *RILEM Tech. Lett.* **2022**, *7*, 98–111. [CrossRef]
5. Yang, M.; Li, S.; Ma, Y.; Tan, Y.; Zhang, Y. Evaluation of chloride effects on sulfate attack in cement paste: Insights into phase composition and micromechanical degradation across corrosion depths. *J. Build. Eng.* **2026**, *129*, 116755. [CrossRef]
6. Cheng, S.; Wu, Z.; Wu, Q.; Chen, X.; Shui, Z.; Lu, J.-X. Degradation characteristics of Portland cement mortar incorporating supplementary cementitious materials under multi-ions attacks and drying-wetting cycles. *J. Clean. Prod.* **2022**, *363*, 132378. [CrossRef]
7. Yang, B.; Chen, Y.; Jiang, C.; Chen, G.; Maimaiti, A. Degradation mechanism of low-heat Portland cement paste under semi-immersion magnesium sulfate attack with wetting–drying cycles. *Materials* **2026**, *19*, 4373. [CrossRef] [PubMed]
8. Du, S.; Zhao, Q.; Shi, X. Quantification of the reaction degree of fly ash in blended cement systems. *Cem. Concr. Res.* **2023**, *167*, 107121. [CrossRef]
9. Afridi, S.; Sikandar, M.A.; Waseem, M.; Nasir, H.; Naseer, A. Chemical durability of superabsorbent polymer (SAP) based geopolymer mortars (GPMs). *Constr. Build. Mater.* **2019**, *217*, 530–542. [CrossRef]
10. Xing, M.; Chen, H.; Xu, A.; Chen, H.; Zheng, S.; Sun, Y. Moisture regulation, performance influence, and synergistic strategies of superabsorbent polymers in cement-based materials: A comprehensive review. *Int. J. Concr. Struct. Mater.* **2026**, *20*, 66. [CrossRef]
11. Zhang, X.; Li, G.; Yan, J.; Yu, Y.; Li, N.; Jin, Z. The design of an organic-inorganic composite superabsorbent polymer with modified fly ash as rigid support and its regulation on cement hydration and microstructure. *Constr. Build. Mater.* **2026**, *522*, 146245. [CrossRef]
12. Tan, Y.; Chen, H.; Wang, Z.; Xue, C.; He, R. Performances of cement mortar incorporating superabsorbent polymer (SAP) using different dosing methods. *Materials* **2019**, *12*, 1619. [CrossRef] [PubMed]
13. Van Mullem, T.; De Brabandere, L.; Van de Voorde, E.; Snoeck, D.; De Belie, N. Influence of superabsorbent polymers on the chloride ingress of mortar measured by chloride diffusion and a quasi-steady-state migration test. *Cem. Concr. Compos.* **2024**, *150*, 105563. [CrossRef]
14. Gupta, S. Effect of presoaked superabsorbent polymer on strength and permeability of cement mortar. *Mag. Concr. Res.* **2018**, *70*, 473–486. [CrossRef]
15. Tu, W.; Zhu, Y.; Fang, G.; Wang, X.; Zhang, M. Internal curing of alkali-activated fly ash-slag pastes using superabsorbent polymer. *Cem. Concr. Res.* **2019**, *116*, 179–190. [CrossRef]
16. Lyu, J.; Feng, S. Effect of superabsorbent polymers (SAPs) and fly ash on mechanical properties and microstructure of mortar. *J. Sustain. Cem.-Based Mater.* **2024**, *14*, 1–18. [CrossRef]
17. Li, L.; Yu, Z.; Xia, X.; Zhang, X.; Liu, Z.; Shi, Q. Temperature-dependent durability assessment of fly-ash concrete under coupled chloride-sulfate attack. *Constr. Build. Mater.* **2026**, *545*, 148378. [CrossRef]
18. Zhao, G.; Ding, Y.; Wang, C.; Ni, X.; Chen, L.; Zhang, C.; Bao, L.; Wei, F. Durability performance of cast-in-situ mortar containing iron tailings sand under synergistic internal-external sulfate, chloride, and magnesium attack. *J. Sustain. Cem.-Based Mater.* **2026**, *15*, 1915–1933. [CrossRef]
19. Sotiriadis, K.; Hlobil, M.; Viani, A.; Mácová, P.; Vopálenský, M. Physical-chemical-mechanical quantitative assessment of the microstructural evolution in Portland-limestone cement pastes exposed to magnesium sulfate attack at low temperature. *Cem. Concr. Res.* **2021**, *149*, 106566. [CrossRef]

20. Kim, I.; Choi, S.; Choi, Y.; Yang, E. Effect of internal pores formed by a superabsorbent polymer on durability and drying shrinkage of concrete specimens. *Materials* **2021**, *14*, 5199. [CrossRef] [PubMed]
21. Jiang, Q.; Wan, K. Improving internal curing efficiency through adjusting ab- and desorption curve of superabsorbent polymer in cement pastes using sodium carbonate. *Cem. Concr. Compos.* **2022**, *129*, 104467. [CrossRef]

Disclaimer/Publisher's Note: The statements, opinions and data contained in all publications are solely those of the individual author(s) and contributor(s) and not of MDPI and/or the editor(s). MDPI and/or the editor(s) disclaim responsibility for any injury to people or property resulting from any ideas, methods, instructions or products referred to in the content.